

Supporting information

ZnO/Co₃O₄ supported on carbon nanotubes as anode materials for high-performance lithium-ion batteries

Songli Qiu, Jiafeng Wu, Liyu Chen,* Yingwei Li*

Guangdong Provincial Key Laboratory of Fuel Cell Technology, School of Chemistry and Chemical Engineering, South China University of Technology, Guangzhou 510640, China.

Email: liyuchen@scut.edu.cn; liyw@scut.edu.cn.

Experiment section

1. Chemicals

Cobalt acetate hexahydrate ($\text{Co}(\text{OAc})_2 \cdot 4\text{H}_2\text{O}$, 99.9%), zinc acetate dihydrate ($\text{Zn}(\text{OAc})_2 \cdot 2\text{H}_2\text{O}$, 99.9%), 2-methylimidazole ($\text{C}_4\text{H}_6\text{N}_2$, 99%), and n-butylamine ($\text{CH}_3(\text{CH}_2)_3\text{NH}_2$) were purchased from Aladdin. All chemicals and solvents were used without any further purification.

2. Preparation of Zn/Co-ZIF

First, 0.821 g of 2-methylimidazole and 1.2 mL of n-butylamine were dissolved in 40 mL of deionized water under stirring to form solution A. Solutions B and C were prepared by dissolving 0.219 g of $\text{Zn}(\text{OAc})_2 \cdot 2\text{H}_2\text{O}$ and 0.249 g $\text{Co}(\text{OAc})_2 \cdot 4\text{H}_2\text{O}$, respectively, in 10 mL of deionized water each. Solutions B and C were then combined with solution A and mixed uniformly at room temperature. A purple precipitate was formed, which was washed three times with deionized water and ethanol, and then dried at 60 °C for 12 hours to obtain Zn/Co-ZIF. ZIF-67 was prepared using the same procedure, substituting $\text{Zn}(\text{OAc})_2 \cdot 2\text{H}_2\text{O}$ with $\text{Co}(\text{OAc})_2 \cdot 4\text{H}_2\text{O}$ in solution B.

3. Preparation of ZnO/Co₃O₄@CNTs

The freshly prepared Zn/Co-ZIF was transferred to a tube furnace and annealed at 400 °C with a heating rate of 1 °C/min for 2 hours. Subsequently, it was heated to 800 °C at a rate of 2 °C/min for 1.5 hours to complete a two-step carbonization process under an H_2/Ar atmosphere. The final product was obtained by oxidizing the intermediate product in an air environment at 400 °C with a heating rate of 2 °C/min for different time of 5, 10, 15, and 20 minutes, yielding ZnO/Co₃O₄@CNTs-5, ZnO/Co₃O₄@CNTs, ZnO/Co₃O₄@CNTs-15, and ZnO/Co₃O₄@CNTs-20, respectively.

4. Preparation of ZnO/Co₃O₄@C, ZnO/Co₃O₄, and Co₃O₄@CNTs

Zn/Co-ZIF was placed into a tube furnace and heated up to 800 °C at a rate of 2 °C/min in the H_2/Ar atmosphere for 2 hours to obtain Zn/Co@C. After cooling to room temperature, Zn/Co@C was oxidized at 400 °C for 10 minutes with a ramp rate of 2 °C/min in air to form ZnO/Co₃O₄@C.

ZnO and Co₃O₄ bimetallic oxide (denoted as ZnO/Co₃O₄) was prepared by oxidizing Zn/Co-ZIF at 600 °C with a heating rate of 2 °C/min for 4 hours in air.

Co₃O₄@CNTs was obtained following the preparation process of ZnO/Co₃O₄@CNTs by using ZIF-67 as a precursor instead of Zn/Co-ZIF.

5. Material characterization

The surface topography, internal structure, and elemental composition and distribution were analyzed using Field emission scanning electron microscopy (FE-SEM, HITACHI, SU8100), transmission electron microscope (TEM, JEOL, JEM-2100F), and energy dispersive spectrometer (EDS). Structural analysis was performed using an X-ray diffractometer (XRD, Rigaku, D/MAX/III A) with Cu K α radiation. Elemental composition and chemical state characterization were conducted using X-ray photoelectron spectroscopy (XPS, Thermo Fisher Scientific, K-Alpha). Porosity and specific surface area were determined using an accelerated surface area and porosimetry system (Micromeritics ASAP 2460). Raman spectra were recorded on a LabRAM HR system (Horiba Jobin Yvon) by applying a 633 nm laser. The thermal stability of the materials was analyzed using a thermogravimetric analyzer (TGA, Netzsch TG209F1). Surface potential and work function were measured using Kelvin probe force microscopy (KPFM, BRUKER, Dimension Icon).

6. Electrochemical measurements

The battery was assembled using a CR2025 case, with a lithium sheet as the counter electrode and Celgard 2400 microporous polypropylene as the separator. The working electrode was prepared by mixing the active material, conductive carbon black, and polyvinylidene fluoride (PVDF) in an 8:1:1 (the total mass is 100 mg). This mixture was combined with the polar solvent N-Methyl-2-pyrrolidone (NMP) in an agate mortar, thoroughly mixed, and then uniformly coated onto a copper foil. The coated foil was cut into suitable electrode plates using a punching machine, achieving a load mass density of 0.8–1.3 mg cm⁻². The electrolyte solution comprised 1 M LiPF₆ evenly dispersed in a mixture of ethylene carbonate (EC), dimethyl carbonate (DMC), and ethyl methyl carbonate (EMC) in a 1:1:1 volume ratio, with an additional 1% vinylene carbonate (VC).

To supply an adequate lithium source for the formation of the solid electrolyte interphase (SEI) and enhance electrode stability, pre-lithiation anode materials were prepared using an electrochemical pre-lithiation technique. This involved five cycles at a low current density of 100 mA g^{-1} over a voltage range of 0.01–3 V. Instead of using lithium metal foil, commercial lithium iron phosphate (LiFePO_4 , LFP) was used as the cathode, with a loading density of approximately $9.2\text{--}15 \text{ mg cm}^{-2}$ and negative/positive (N/P) proportions between 1.05 and 1.2.

Constant current charge/discharge tests were conducted using a LAND CT2001A battery testing apparatus. Voltage windows were set at 0.01–3.0 V for anodes and 1.0–3.5 V for full cells. Cyclic voltammetry (CV) measurements were performed on an electrochemical workstation (CHI 760E) within a voltage range of 0.01–3.0 V, with scan rates varying from $0.2\text{--}0.8 \text{ mV s}^{-1}$. Electrochemical impedance spectroscopy (EIS) was conducted over a frequency range of $10^{-1}\text{--}10^5 \text{ Hz}$. The galvanostatic intermittent titration technique (GITT) was performed with a single current pulse lasting two minutes, followed by a ten-minute rest period, within a voltage range of 0.1–2.5 V at a current of 0.02 mA.

7. Mechanism investigation

7.1 *b* values calculation

Capacitive behavior refers to charge storage processes occurring at the electrode material's surface, and diffusion-controlled behavior involves reactions within the active material constrained by the rate of ion diffusion through the electrolyte. The following formulas are available to identify its type:

$$i = av^b \quad (1)$$

$$\log i = b \log v + \log a \quad (2)$$

The coefficients, peak currents, and scan rates are denoted as *a*, *i*, and *v*, respectively. It is necessary to determine the dominant mechanism (*b* values) by conducting linear fittings of $\log i$ and $\log v$. When *b* equals to 0.5 or 1, the mechanism is judged as diffusive or capacitive behavior, respectively.

7.2 Capacitance contribution ratio calculation

The equations shown below are applied to acquire greater accuracy on the capacitance contribution ratio:

$$i = k_1v + k_2v^{1/2} \quad (3)$$

$$i/v^{1/2} = k_1v^{1/2} + k_2 \quad (4)$$

The correlation between $i/v^{1/2}$ and $v^{1/2}$ was used to ascertain the values of k_1 and k_2 . The k_1v and $k_2v^{1/2}$ represent the capacitive-controlled and diffusion-controlled contributions, respectively. The typical CV profiles from capacitive (pink area) and diffusion-dominated processes (blue area) at 0.2, 0.4, 0.6, and 0.8 mV s^{-1} of different samples are shown in Figures 3h and S18–21. The pseudocapacitance contributions were calculated by the ratio of pink area/blue area at scan rates of 0.2, 0.4, 0.6, and 0.8 mV s^{-1} .

7.3 Work function calculation

Using highly oriented pyrolytic graphite (HOPG) as the standard sample, a bias voltage is applied to the probe, and the contact potential difference CPD (contact potential difference) is calculated using the formula:

$$CPD = P_{sample} - P_{probe} \quad (5)$$

P_{Sample} and P_{Probe} are the potentials of the sample and probe. Work function is determined by the following formula:

$$eP_{sample} - eP_{probe} = eV_{probe} - eV_{sample} \quad (6)$$

Where, eV_{probe} and eV_{sample} represent the work function of the probe and sample, respectively.

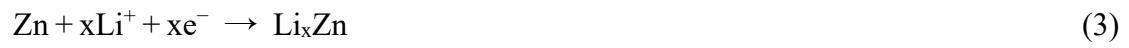
7.4 Lithium ion (Li^+) diffusion coefficients calculation

GITT tests were performed to calculate the Li^+ diffusion coefficients of the materials based on Fick's second law (Fig. 4g and S27):

$$D = \frac{4}{\pi\tau} \left\{ \frac{m_B V_m}{M_B S} \right\}^2 \left\{ \frac{\Delta E_S}{\Delta E\tau} \right\}^2 \quad (7)$$

τ , ΔE_S , and $\Delta E\tau$ stand for the pulse time, voltage variation, and total voltage variation, respectively, and m_B , M_B , V_m , and S are the electrode material relevant parameters.

8. Electrochemical reactions

Discharge:**Charge:**

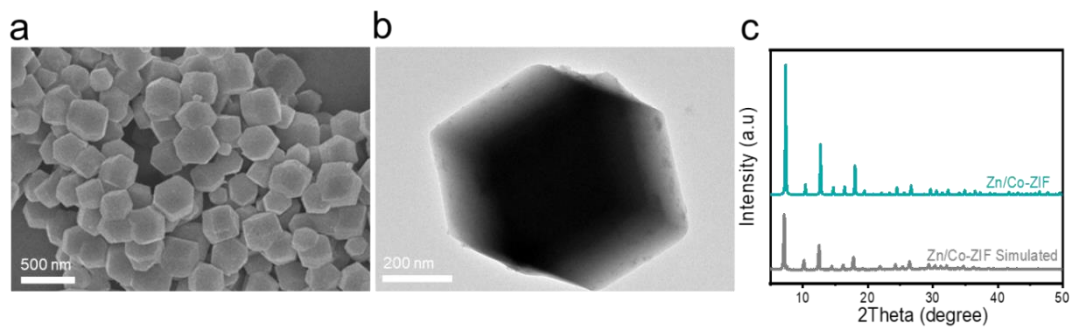


Fig. S1 (a) SEM image, (b) TEM image, and (c) XRD pattern of Zn/Co-ZIF.

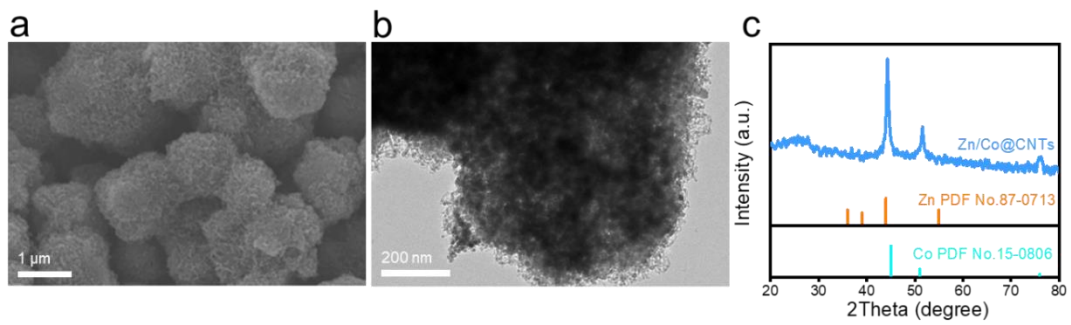


Fig. S2 (a) SEM image, (b) TEM image, and (c) XRD pattern of Zn/Co@CNTs.

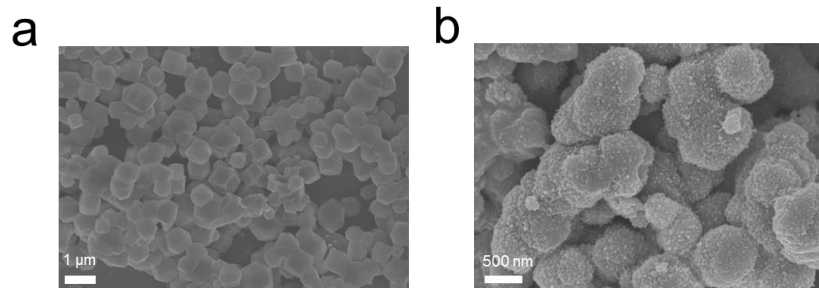


Fig. S3 SEM images of (a) Zn/Co-ZIF calcined at 400 °C for 2 hours and (b) Zn/Co@C.

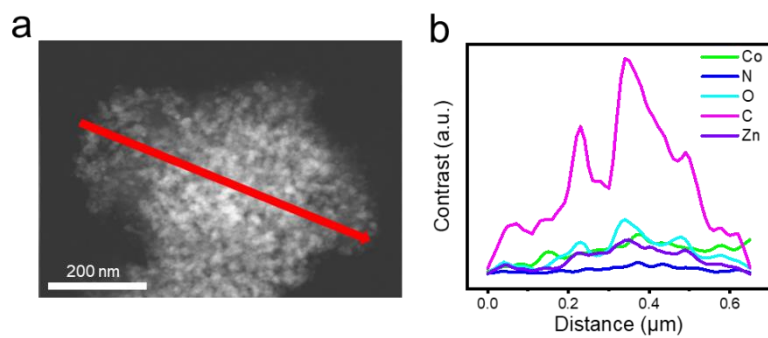


Fig. S4 (a) HAADF-STEM image and (b) elemental line scan profiles of ZnO/Co₃O₄@CNTs.

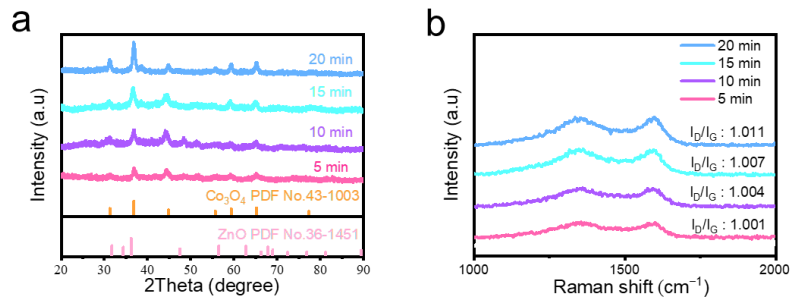


Fig. S5 (a) XRD patterns and (b) Raman spectra of ZnO/ Co_3O_4 @CNTs with oxidation time of 5, 10, 15, and 20 min.

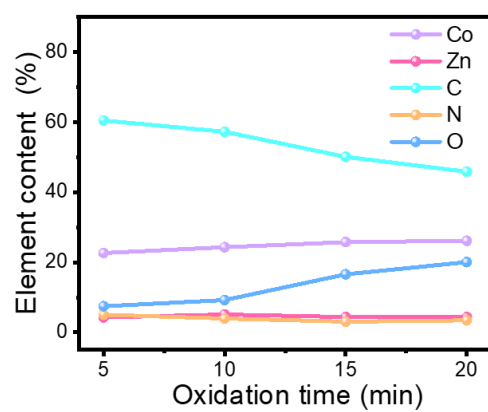


Fig. S6 The variations of element content with oxidation time.

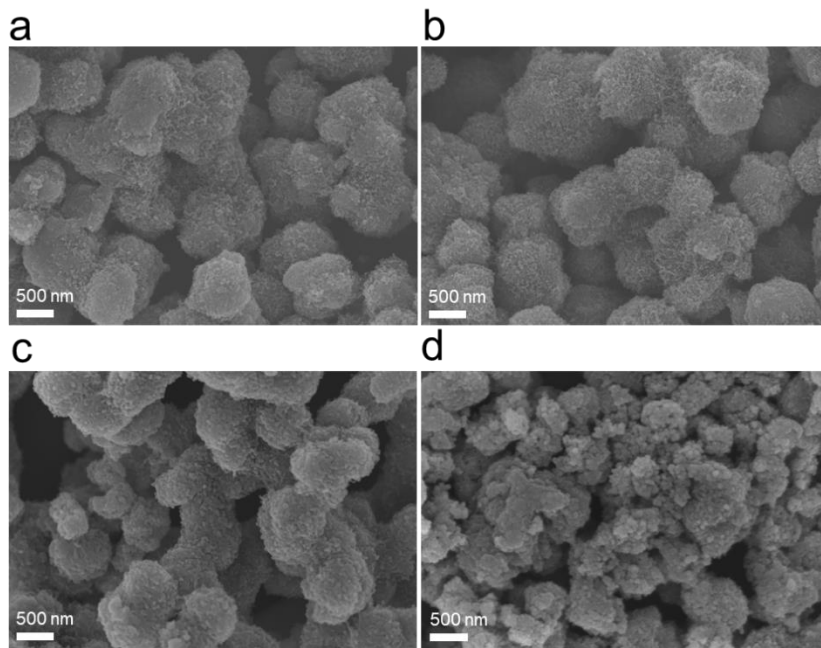


Fig. S7 SEM images of ZnO/Co₃O₄@CNTs with an oxidation time of (a) 5, (b) 10, (c) 15, and (d) 20 min.

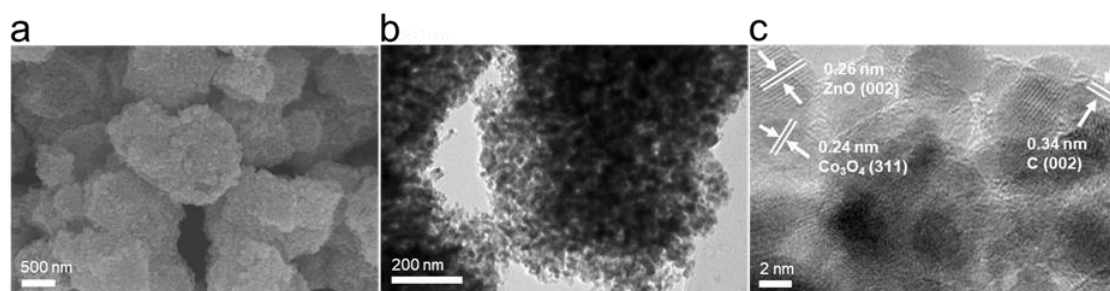


Fig. S8 (a) SEM image, (b) TEM image, and (c) HRTEM image of ZnO/Co₃O₄@C.

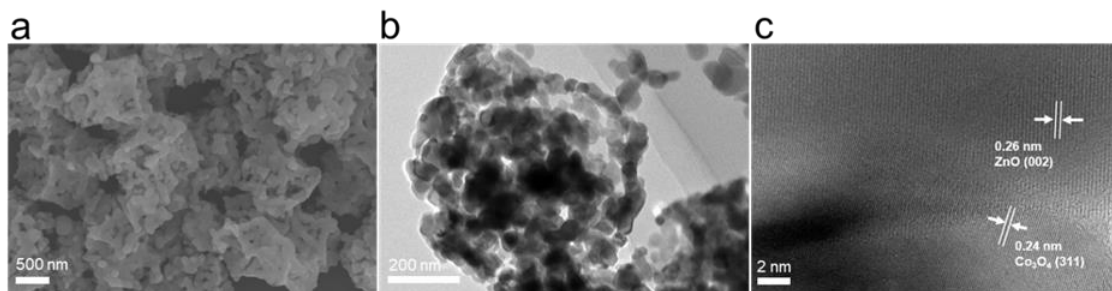


Fig. S9 (a) SEM image, (b) TEM image, and (c) HRTEM image of ZnO/Co₃O₄.

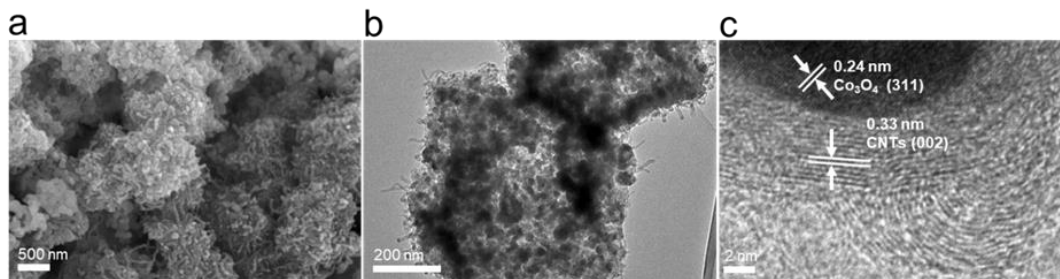


Fig. S10 (a) SEM image, (b) TEM image, and (c) HRTEM image of Co_3O_4 @CNTs.

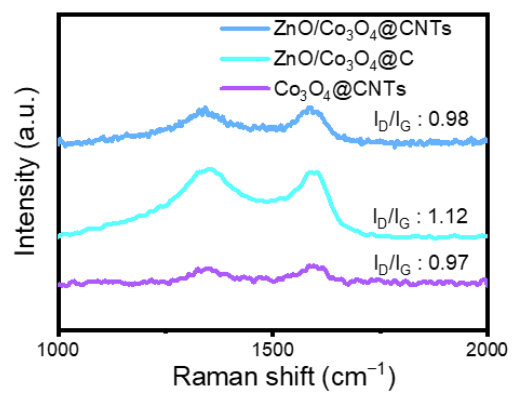


Fig. S11 Raman spectra of ZnO/Co₃O₄@CNTs, ZnO/Co₃O₄@C, and Co₃O₄@CNTs.

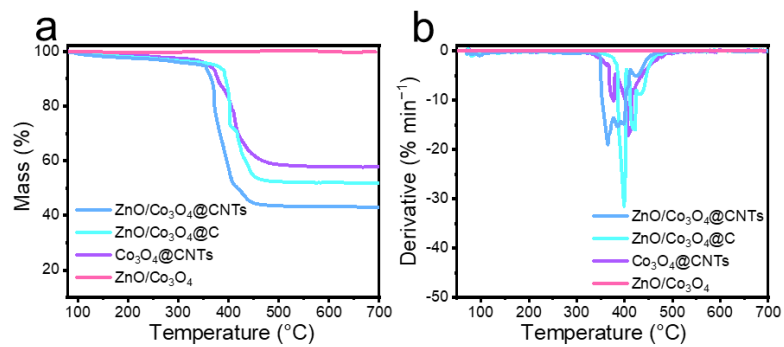


Fig. S12 (a) The TGA curves and (b) DTG curves of ZnO/Co₃O₄@CNTs, ZnO/Co₃O₄@C, Co₃O₄@CNTs, and ZnO/Co₃O₄.

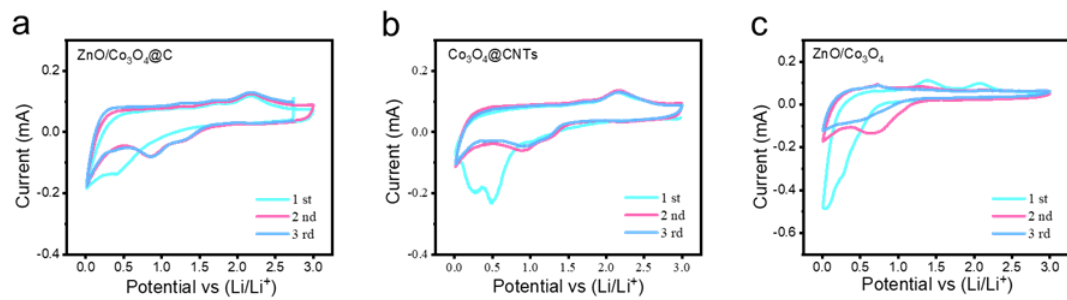


Fig. S13 CV curves of (a) ZnO/Co₃O₄@C, (b) Co₃O₄@CNTs, and (c) ZnO/Co₃O₄ at the scan rate of 0.2 mV s⁻¹.

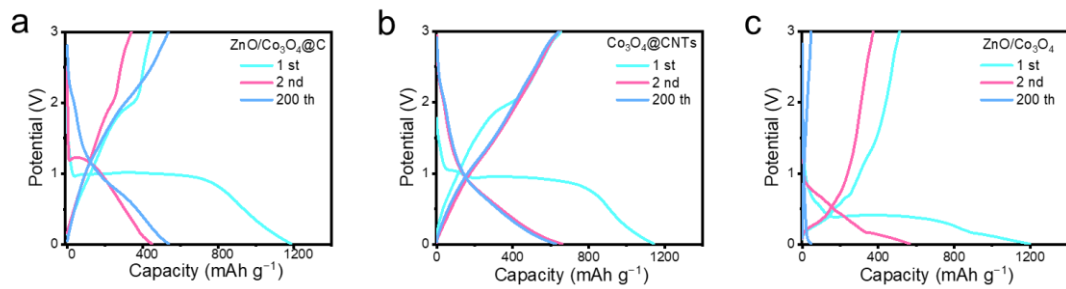


Fig. S14 The galvanostatic discharge/charge curves of (a) ZnO/Co₃O₄@C, (b) Co₃O₄@CNTs, and (c) ZnO/Co₃O₄ at the current density of 200 mAh g⁻¹.

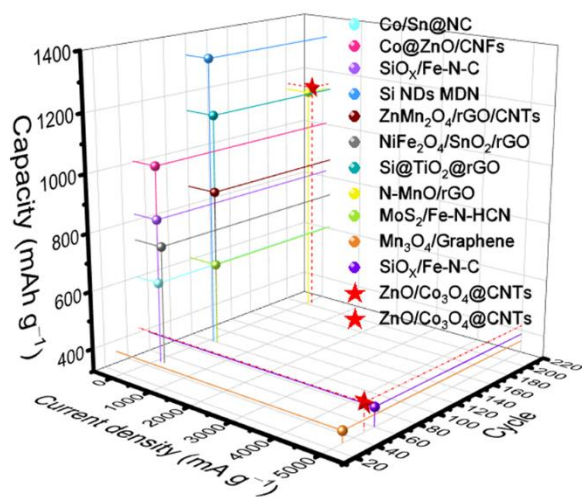


Fig. S15 Comparisons of the electrochemical performances of $\text{ZnO/Co}_3\text{O}_4@\text{CNTs}$ with other carbon-based composite materials for LIBs.

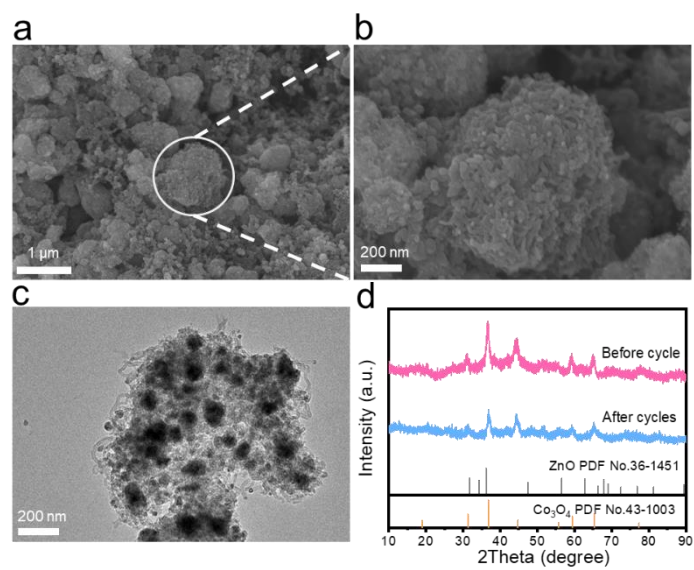


Fig. S16 (a, b) SEM images, (c) TEM image, and (d) XRD patterns of ZnO/Co₃O₄@CNTs after 200 cycles at 200 mA g⁻¹.

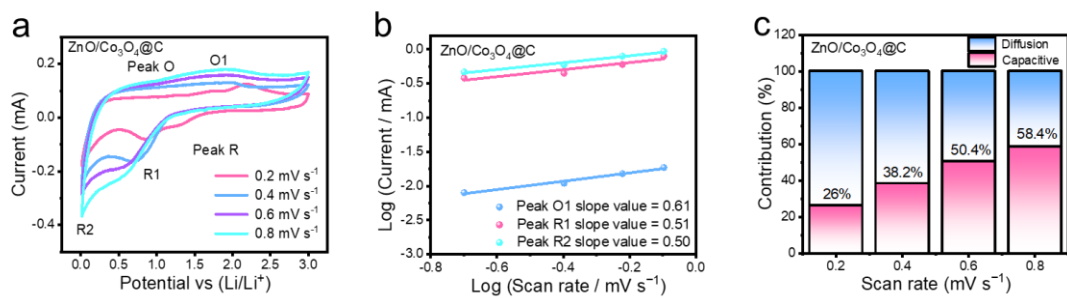


Fig. S17 (a) CV curves at different scan rates from 0.2 to 0.8 mV s⁻¹, (b) the b-value calculated from plotting the peak current versus scan rate, and (c) contribution ratio of capacitive capacity at different scan rates of ZnO/Co₃O₄@C.

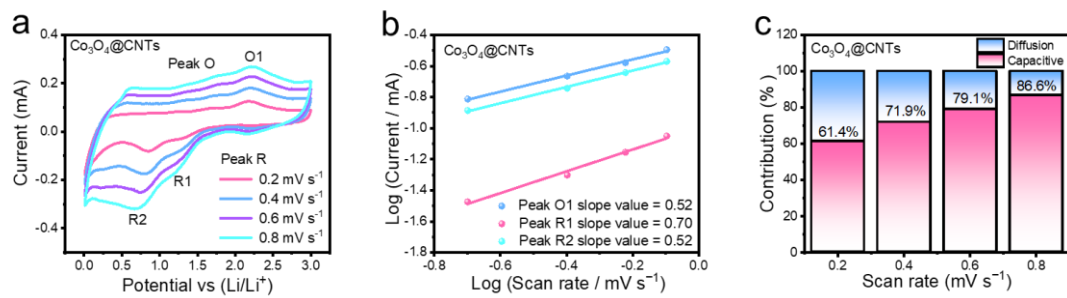


Fig. S18 (a) CV curves at different scan rates from 0.2 to 0.8 mV s⁻¹, (b) the b-value calculated from plotting the peak current versus scan rate, and (c) contribution ratio of capacitive capacity at different scan rates of Co₃O₄@CNTs.

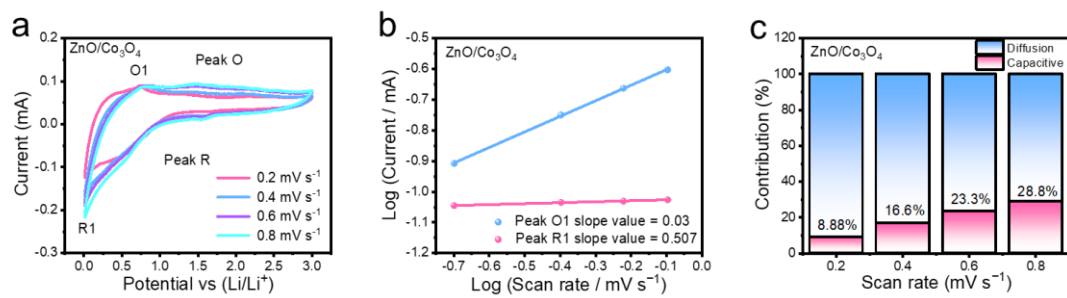


Fig. S19 (a) CV curves at different scan rates from 0.2 to 0.8 mV s⁻¹, (b) the b-value calculated from plotting the peak current versus scan rate, and (c) contribution ratio of capacitive capacity at different scan rates of ZnO/Co₃O₄.

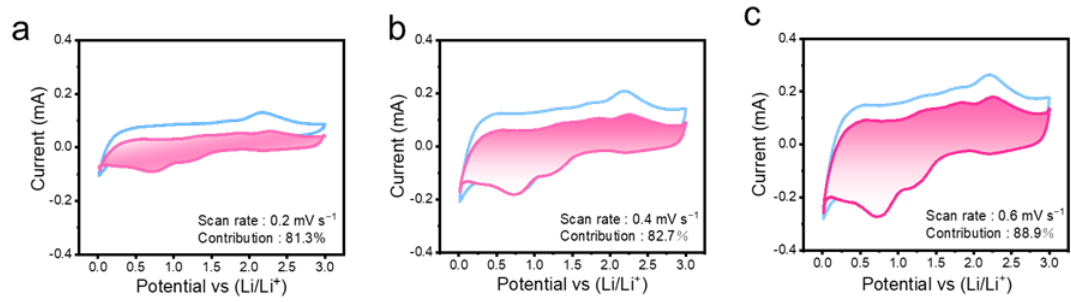


Fig. S20 The contribution ratios of capacitive capacity of ZnO/Co₃O₄@CNTs at (a) 0.2 mV s⁻¹, (b) 0.4 mV s⁻¹, (c) 0.6 mV s⁻¹.

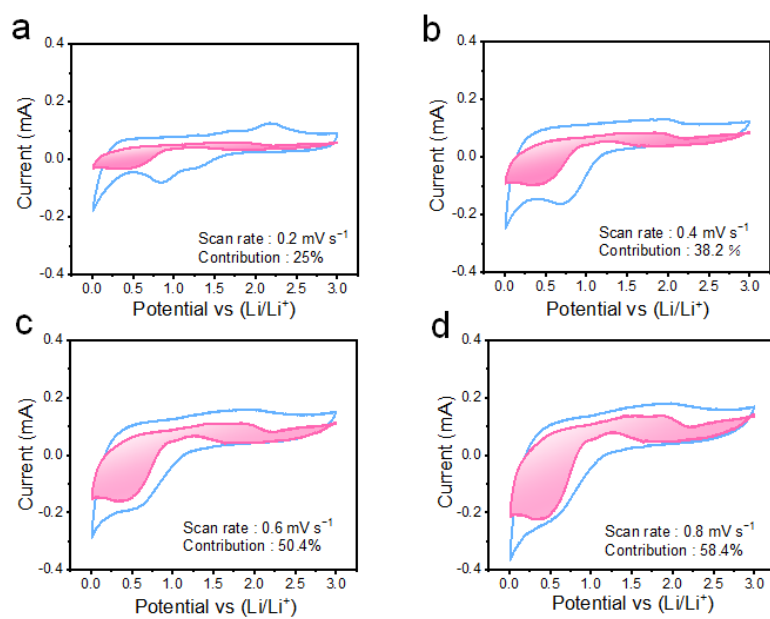


Fig. S21 The contribution ratios of capacitive capacity of ZnO/Co₃O₄@C at scan rates of (a) 0.2, (b) 0.4, (c) 0.6, (d) 0.8 mV s⁻¹.

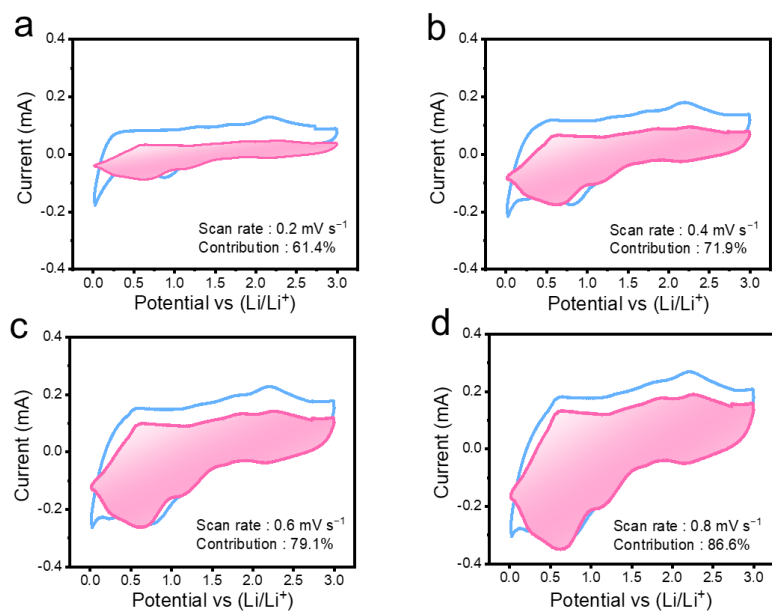


Fig. S22 The contribution ratios of capacitive capacity of $\text{Co}_3\text{O}_4@\text{CNTs}$ at scan rates of (a) 0.2, (b) 0.4, (c) 0.6, (d) 0.8 mV s^{-1} .

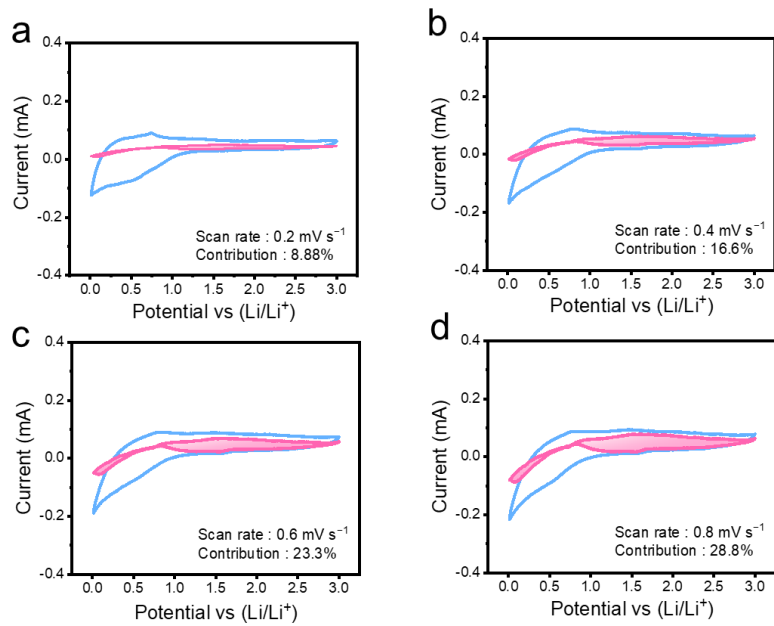


Fig. S23 The contribution ratios of capacitive capacity of ZnO/Co₃O₄ at scan rates of (a) 0.2, (b) 0.4, (c) 0.6, (d) 0.8 mV s⁻¹.

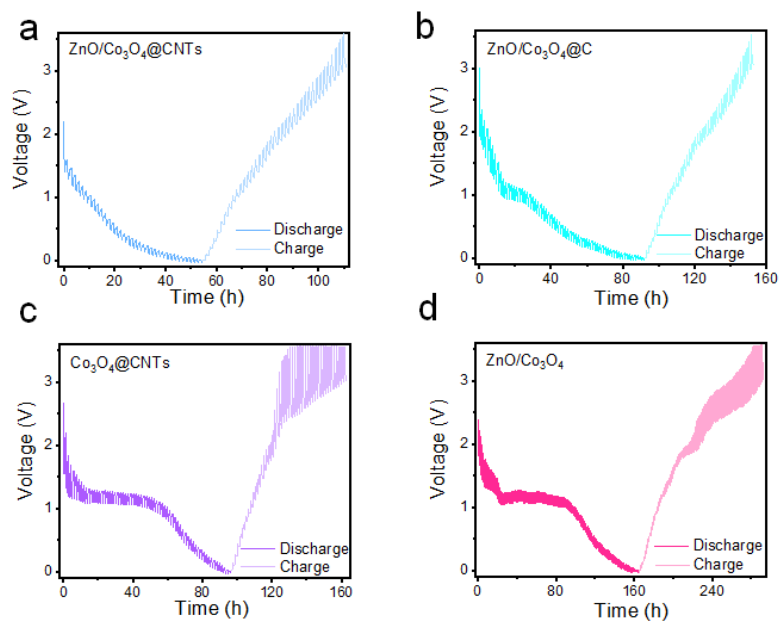


Fig. S24 GITT plots of LIBs with (a) ZnO/Co₃O₄@CNTs, (b) ZnO/Co₃O₄@C, (c) Co₃O₄@CNTs, and (d) ZnO/Co₃O₄ in the first discharge/charge process under the current density of 0.02 mA g⁻¹.

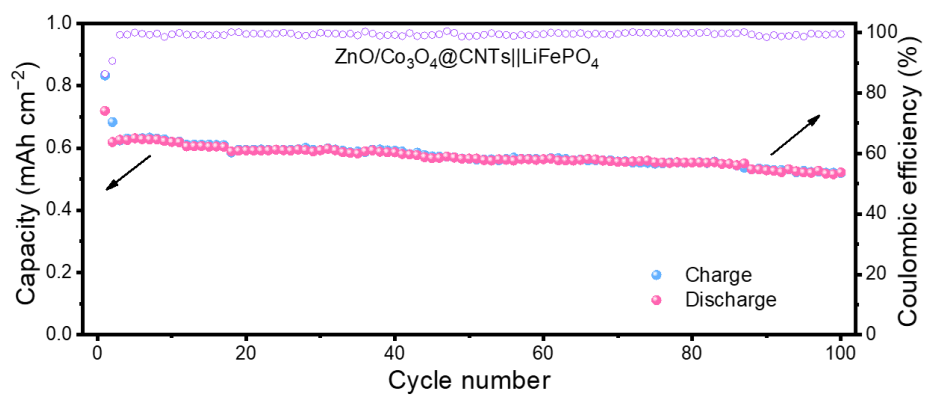


Fig. S25 The cycling performance based on area capacity calculation of the full cell of ZnO/Co₃O₄@CNTs || LFP at the current density of 0.2 C.

Table S1 The contents of Zn and Co in ZnO/Co₃O₄@CNTs

Element	Content (wt%)
Zn	4.2
Co	32.11

Table S2 Comparisons of cycling performances of ZnO/Co₃O₄@CNTs with other carbon-based composite materials for LIBs

Active materials	Current density (mA g ⁻¹)	Initial capacity (mAh g ⁻¹)	Capacity (mAh g ⁻¹) (cycles)	Ref.
Co/Sn@NC	100	1002	601 (50)	1
Co@ZnO/CNFs	100	1738	1004.9 (50)	2
SiO _x /Fe-N-C	100	1227	821.9 (50)	3
Si NDs MDN	100	1592	1327 (100)	4
ZnMn ₂ O ₄ /rGO/CNTs	200	1260	867 (100)	5
NiFe ₂ O ₄ /SnO ₂ /rGO	200	1450	732 (50)	6
Si@TiO ₂ @rGO	200	1855	1135.1 (100)	7
N-MnO/rGO	200	1281	920 (100)	8
MoS ₂ /Fe-N-HCN	200	757	607 (100)	9
Mn ₃ O ₄ /Graphene	5000	-	361 (30)	10
SiO _x /Fe-N-C	5000	-	386.2 (60)	3
ZnO/Co ₃ O ₄ @CNTs	5000	-	417.5 (50)	This work
ZnO/Co ₃ O ₄ @CNTs	200	1460	1156 (200)	This work

Table S3 Various resistances of different materials

Samples	R_e/Ω	R_{SEI}/Ω	R_{ct}/Ω	Z_w/Ω
ZnO/Co ₃ O ₄ @CNTs	4.85	36.15	83.12	0.40
ZnO/Co ₃ O ₄ @C	5.03	90.23	100.63	0.46
Co ₃ O ₄ @CNTs	5.67	50.68	96.52	0.41
ZnO/Co ₃ O ₄	6.25	151.45	145.27	0.51

Table S4 Comparisons of D (Li^+) among different composites ($\text{cm}^2 \text{s}^{-1}$)

Samples	Discharge (10^{-9})	Charge (10^{-9})	Average (10^{-9})
ZnO/Co ₃ O ₄ @CNTs	1.02	1.18	1.1
ZnO/Co ₃ O ₄ @C	0.104	0.702	0.421
Co ₃ O ₄ @CNTs	0.255	0.915	0.558
ZnO/Co ₃ O ₄	0.081	0.565	0.323

Table S5 Data for calculating the work function of ZnO/Co₃O₄@CNTs

Test subjects	Contact potential difference (V)	Work function (eV)
Probe	-	4.959
Highly oriented pyrolytic graphite (HOPG)	0.359	4.6
ZnO/Co ₃ O ₄ @CNTs	0.876	4.083

Table S6 Data for calculating the work function of ZnO/Co₃O₄@C

Test subjects	Contact potential difference (V)	Work function (eV)
Probe	-	4.959
Highly oriented pyrolytic graphite (HOPG)	0.359	4.6
ZnO/Co ₃ O ₄ @C	0.813	4.146

Reference

1. S. Ashraf, R. Mehek, N. Iqbal, T. Noor, G. Ali, A. Wahab, A. A. Qayyum and A. Ahmad, *Mater. Chem. Phys.*, 2021, **270**, 124824.
2. J. Peng, J. Tao, Z. Liu, Y. Yang, L. Yu, M. Zhang, F. Wang and Y. Ding, *Chem. Eng. J.*, 2021, **417**, 129200.
3. X. Guo, H. Xu, W. Li, Y. Liu, Y. Shi, Q. Li and H. Pang, *Adv. Sci.*, 2022, **10**, 2206084.
4. B. Chen, L. Chen, L. Zu, Y. Feng, Q. Su, C. Zhang and J. Yang, *Adv. Mater.*, 2022, **34**, 2200894.
5. Q. Tang, Y. Shi, Z. Ding, T. Wu, J. Wu, V. Mattick, Q. Yuan, H. Yu and K. Huang, *Electrochim. Acta*, 2020, **338**, 135853.
6. H. Shen, X. Xia, S. Yan, X. Jiao, D. Sun, W. Lei and Q. Hao, *J. Alloys Compd.*, 2021, **853**, 157017.
7. R. Fang, C. Miao, H. Mou and W. Xiao, *J. Alloys Compd.*, 2020, **818**, 152884.
8. X.-Y. Pei, D.-C. Mo, S.-S. Lyu, J.-H. Zhang and Y.-X. Fu, *Appl. Surf. Sci.*, 2019, **465**, 470–477.
9. J. Ren, H. Guo, Z. Wang, G. Ling, J. Han, R.-P. Ren and n. Yongkang-Lv, *J. Colloid Interface Sci.*, 2024, **664**, 45–52.
10. B.-L. Yan, D. Jun, J. Wang, T. Yang and X.-H. Mao, *J. Alloys Compd.*, 2022, **905**, 164121.